ACS OMEGA

http://pubs.acs.org/journal/acsodf

Article

Kinetics and Thermodynamics Study of Methylene Blue Adsorption to Sucrose- and Urea-Derived Nitrogen-Enriched, Hierarchically Porous Carbon Activated by KOH and H_3PO_4

Heshan Liyanaarachchi, Charitha Thambiliyagodage,* Hasindhi Lokuge, and Saravanamuthu Vigneswaran

Cite This: *ACS Omega* 2023, 8, 16158−16173

Read Online

ACCESS | Metrics & More | Article Recommendations | Supporting Information

ABSTRACT: Hierarchically porous nitrogen-enriched carbon materials synthesized by polymerization of sucrose and urea (SU) were activated by KOH and H_3PO_4 (SU-KOH and SU-H_3PO_4, respectively). Characterization was undertaken and the synthesized materials were tested for their ability to adsorb methylene blue (MB). Scanning electron microscopic images along with the Brunauer−Emmett−Teller (BET) surface area analysis revealed the presence of a hierarchically porous system. X-ray photoelectron spectroscopy (XPS) confirms the surface oxidation of SU upon activation with KOH and H_3PO_4. The best conditions for removing dyes utilizing both activated adsorbents were determined by varying the pH, contact time, adsorbent dosage, and dye concentration. Adsorption kinetics were evaluated, and the adsorption of MB followed second-order kinetics, suggesting the chemisorption of MB to both SU-KOH and SU-H_3PO_4. Times taken to reach the equilibrium by SU-KOH and SU-H_3PO_4 were 180 and 30 min, respectively. The adsorption isotherm data were fitted to the Langmuir, Freundlich, Temkin, and Dubinin models. Data were best described by the Temkin isotherm model for SU-KOH and the Freundlich isotherm model for SU-H_3PO_4. Thermodynamics of the adsorption of MB to the adsorbent was determined by varying the temperature in the range of 25−55 °C. Adsorption of MB increased with increasing temperature, suggesting that the adsorption process is endothermic. The highest adsorption capacities of SU-KOH and SU-H_3PO_4 (1268 and 897 mg g^{-1}, respectively) were obtained at 55 °C. Synthesized adsorbents were effective in removing MB for five cycles with some loss in activity. The results of this study show that SU activated by KOH and H_3PO_4 are environmentally benign, favorable, and effective adsorbents for MB adsorption.

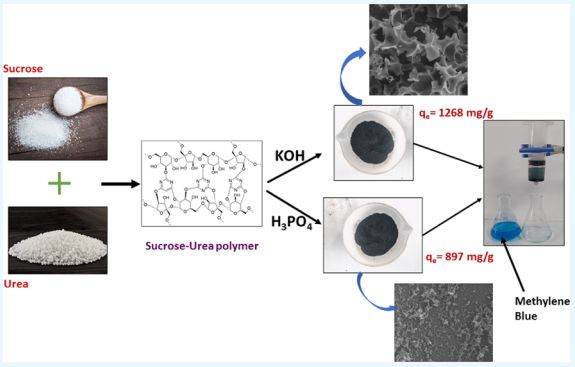

1. INTRODUCTION

Water scarcity as a consequence of the creation of wastewater has not been helped by the rapid growth of industries that now use a lot of the earth's water, and this practice threatens the well-being of all people, flora, and fauna. Dyes released from many industries including textiles, paints, paper, cosmetics, pharmaceuticals, etc., are considered major pollutants that destroy the quality of water required for safe domestic and industrial purposes. Dyes are more recalcitrant to biodegradation due to their complex chemical nature and hence get accumulated, creating severe hazardous outcomes including an increase in the biological oxygen demand, an increase in the chemical oxygen demand,[1] severe damage done to aquatic living beings due to the heavy metals, chlorinated compounds, surfactants released with dyes[2−4] decline in the photosynthesis due to the limited light penetration,[5] and deteriorating the aesthetic value of the planet's finite water bodies.[6] Hence, it is vital to remove dyes from water reservoirs. There are many methods available for such purposes including membrane filtration,[7] nanofiltration,[8] adsorption,[9] remediation by microorganisms,[10] ion exchange,[10] ozonation,[11] photooxidation,[12−14] chemical reduction,[15] etc. These methods possess disadvantages such as sludge production, use of expensive chemicals, poor efficiency, short half-life, formation of byproducts, regeneration difficulties,[16] etc.

An ideal dye removal technique should be able to efficiently remove a large number of dyes in a short time without producing secondary pollutants. One such prominent strategy available is adsorption, as it is known to efficiently remove a wide variety of dyes. Many adsorbents have been devised in recent years including silica nanoparticles,[17,18] clay,[8] carbon nanotubes,[10,19] graphene oxide-based composites,[20] metal

Received: January 17, 2023
Accepted: April 20, 2023
Published: April 27, 2023

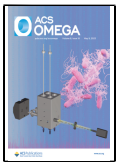

oxides including $MgFe_2O_4$[21] and $ZnO\text{-}Al_2O_3$,[22] metal−organic frameworks such as MIL-53(Al)-NH_2[23] and zirconium-based MOFs,[24] chitosan-based adsorbents,[25] and polymers like polyaniline,[26] polypyrrole,[27] and poly(vinyl alcohol).[28] These substances can remove dyes including methylene blue, bromothymol blue, rhodamine B, Coomassie brilliant blue, Reactive Black 5, methyl orange, Congo red,[29] etc. Carbon-based adsorbents have attracted much scientific attention due to their low cost, high surface area, excellent thermal and electrical stability, hydrophobic surfaces, and tunable textural parameters.[30] Activated carbon is prepared by many sources including agricultural waste such as coconut shells and husk, tea waste, banana peel, coffee husk, corn cob, peanut shells, shrimp shells, etc. Biomass has been activated by employing many activating reagents such as acids like H_3PO_4, HCl, and HNO_3, bases like KOH and NaOH, and salts such as $FeCl_3$ and $ZnCl_2$ to obtain a better performance.

Carbon-based materials have been synthesized using many natural materials including gelatin,[31] pumpkin peels,[32] chicken feathers,[33] tannin,[34] crab shells,[35] shrimp shells,[36] algae,[37] sucrose,[38] glucose,[39] coconut shells,[40] etc. Kundu et al. reported the synthesis of N-doped nonporous carbon using melamine as the precursor, which effectively adsorbed methylene blue.[41] Elsewhere, Zhou et al. discovered that N-containing graphitic mesoporous carbon synthesized using polyacrylonitrile as the precursor could effectively adsorb acid red 88,[42] while Hou et al. reported the preparation of N-doped carbon from bamboo waste to remove methyl orange and rhodamine B.[43] Lone pair electrons on nitrogen incorporated into carbon form electrostatic attractions with dye molecules. N atoms in pyridinic N form H bonds with the dye molecules, further enhancing adsorption. Moreover, especially pyridinic N and pyrrolic N are unlike graphitic N-chemically active and reduce the inertness of carbon by rearranging spin and charge densities producing more active sites.[43,44] N-enriched carbon has been deployed for other uses including capturing CO_2,[45] advanced oxygen electrocatalysis,[46] supercapacitor applications,[47] etc., in addition to adsorbing dyes.

Sucrose is a widely available, commercially viable, and naturally renewable material, while urea is a biomolecule enriched with nitrogen, which is available at a low cost. A combination of sucrose and urea to synthesize an effective adsorbent has not been widely explored. N- and S-doped sucrose-based hierarchically porous carbon has shown to be effective in adsorbing methylene blue and for hydrogen storage.[48] Sucrose- and urea-based N-enriched porous carbon activated by KOH has been used to capture CO_2,[30] and the polymer activated by $ZnCl_2$ is used to adsorb methylene blue.[49] Here, we report the synthesis of sucrose−urea polymer-based N-enriched hierarchically porous carbon by polymerization of sucrose and urea at 250 °C followed by pyrolysis at 800 °C. The obtained carbon material was activated by KOH and H_3PO_4 and they were evaluated on the adsorption of methylene blue. The main objective of this study was to determine the effect of doping of nitrogen and activation by KOH and H_3PO_4 on the adsorption of methylene blue. It emerged that not the enrichment of carbon with N but the textural parameters including the surface area and the macroporosity and the addition of oxygen-rich functional groups through the activation process were responsible for the enhanced adsorption of methylene blue. N-enriched carbon activated by KOH was superior in adsorbing methylene blue than that activated by H_3PO_4. According to our understanding, the adsorption capacities of both activated carbon materials are the highest to what has been reported in the literature for adsorbing methylene blue.

2. MATERIALS AND METHODS

2.1. Chemicals. Sucrose (99.5%) and urea (99.5%) were purchased from Sigma-Aldrich, U.K. H_3PO_4 (88%) was procured from Sigma-Aldrich, Switzerland. KOH (85%) was supplied from Sisco Research Laboratories, India. Methylene blue was purchased from Himedia Laboratories, India.

2.2. Methods. *2.2.1. Preparation of SU.* Sucrose was dissolved in a minimum volume of distilled water and urea dissolved in water was added dropwise where the weight ratio of sucrose to urea was maintained at 1:1. The obtained mixture was heated at 150 °C for 2 h and was increased to 250 °C, subsequently maintaining for 5 h. The product obtained is referred to as SU in the paper's text.

2.2.2. Preparation of SU-KOH. SU was powdered and ground with KOH at a SU/KOH weight ratio of 1:4. The obtained mixture was pyrolyzed at 800 °C for 2 h in N_2 flow. The product obtained was washed with distilled water until the washings were pH neutral and dried at 80 °C. The material is referred to as SU-KOH in the text.

2.2.3. Preparation of SU-H_3PO_4. SU was dispersed in 75 mL of 35 w/v % H_3PO_4 and then stirred at 60 °C for 12 h. The obtained product was washed with distilled water until the pH was neutral, and the dried product was pyrolyzed at 800 °C for 2 h in N_2 flow. The product obtained is referred to as SU-H_3PO_4 in the text.

2.2.4. Effect of pH. The point of zero charge (PZC) of the adsorbents was determined by shaking the adsorbents in a 0.1 M KCl solution in which the initial pH was adjusted to 2, 4, 6, 8, 10, and 12. The final pH was measured after 24 h, and the pH difference was calculated.

The effect of pH on the adsorption of MB to SU, SU-KOH, and SU-H_3PO_4 was determined by varying the pH at 2, 4, 6, 8, 10, and 12 using MB solutions of 25, 500, and 200 mg L^{-1}, respectively. Meanwhile, the weights of the adsorbents used were 25, 10, and 10 mg, respectively. The adsorbents were shaken in MB solutions for 3 h.

2.2.5. Effect of the Weight of the Adsorbent. The weights of both SU-KOH and SU-H_3PO_4 varied in the range of 10−30 mg in 5 mg increments using 50 mL of MB concentrations of 500 and 200 mg L^{-1}, respectively. The adsorbents were shaken with the MB solution for 3 h at room temperature.

2.2.6. Effect of MB Concentration. The MB concentration on the adsorption of MB to the adsorbents was determined by varying the MB concentrations in the 100−500 mg L^{-1} range, in 100 mg L^{-1} increments for SU-KOH. For SU-H_3PO_4, the concentration of MB varied, i.e., 25, 50, 100, 150, and 200 mg L^{-1}. The weights of SU-KOH and SU-H_3PO_4 used were 15 and 10 mg, respectively. The experiments were carried out at room temperature for 3 h.

2.2.7. Effect of Temperature. The adsorption study was carried out by varying the concentration as described in Section 2.2.6 for both SU-KOH and SU-H_3PO_4, and the temperature varied at 25, 35, 45, and 55 °C, using 15 and 10 mg, respectively. The mixture was shaken for 3 h.

3. CHARACTERIZATION

Scanning electron microscopy (SEM) images were obtained by a Carl Zeiss EVO 18 Research spectrophotometer equipped

https://doi.org/10.1021/acsomega.3c00339
ACS Omega 2023, 8, 16158−16173

with an Edax Element EDS system. X-ray diffraction (XRD) patterns were collected via a D8 Advance Bruker system using Cu Kα (λ = 0.154 nm) radiation with varying 2θ from 5 to 80° at a scan speed of 2 ° min^{-1}, and Panalytical software was deployed for analysis. Thermogravimetric analysis was done using an SDTQ600 thermogravimetric analyzer. Analysis was conducted using the room temperature to 800 °C range in a N_2 atmosphere with a ramping rate of 5 °C min^{-1}. Survey spectra and the higher resolution spectra of the synthesized catalysts were acquired by a Thermo Scientific ESCALAB Xi+ X-ray Photoelectron Spectrometer. The instrument was calibrated with pure graphite and the charge was neutralized prior to analysis. Surface area and the pore size distribution were evaluated by a Quantachrome V2.0 instrument, and the samples were degassed at 200 °C for 10 h. The absorbance of MB samples was measured by a Shimadzu UV-1990 double-beam UV−visible spectrophotometer.

4. RESULTS AND DISCUSSION

The sucrose−urea mixtures were homogenized by heating them at 150 °C, and the melts formed brittle foamy solids on heating at 250 °C. The urea in the mixtures is trimerized to produce cyanuric acid when heated at 250 °C and the foaming is caused by the release of ammonia generated during the trimerization and the water vapor created during the condensation. The proposed structure of the polymer is depicted in Figure 1.

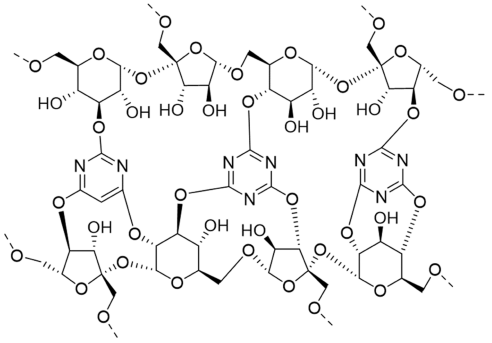

Figure 1. Proposed structure of the polymer formed after heating sucrose and urea.

4.1. SEM Analysis. SEM images (Figure 2) were collected to study the morphology of the adsorbents synthesized. The SEM image of SU (Figure 2a) shows a plane structure where no macropore structure has been developed during the polymerization. As described above, although a foam-like structure was formed during the polymerization due to the release of gaseous molecules produced, it first contributed only to increasing the volume of the substance and second did not create any macropore structure. The SEM image of SU-KOH (Figure 2b) exhibits a well-established macropore structure where the macropores are connected with each other forming channels. Further, as revealed by the Brunauer−Emmett−Teller (BET) analysis, which is discussed in Section 4.4, mesoporous and microporous structures have been well developed, indicating the presence of a hierarchical porous system. Here, the macropores, mesopores, and micropores are interconnected, creating channels and facilitating the migration of solutions containing the adsorbate. This process enables the adsorbates to reach the active sites, and hence, adsorption occurs. However, the walls of some of the macropores are damaged (Figure 2c), creating incomplete pores, which could have occurred during the pyrolysis and washing after carbonization to remove the solid activating agent, KOH. An established macropore structure was not observed in SU-H_3PO_4. However, irregular random small macropores are present, as shown in the SEM image (Figure 2d and the inset). Consequently, it is evident that upon activating carbon with the activating agents, unique macropore structures were established and they contributed to the adsorption of dye molecules immensely.

4.2. XRD Analysis. The XRD patterns of SU, SU-KOH, and SU-H_3PO_4 are shown in Figure 3a, with broad peaks centered at 21.5, 25.6, and 25.3°, respectively. They correspond to the (002) planes of amorphous carbon. A shift in the peak position of 4.1° was observed in SU-KOH compared to SU, and a slight shift compared to SU-KOH was observed in SU-H_3PO_4.

4.3. Thermogravimetric Analysis. Figure 4 shows the thermogravimetric curves of the SU and SU samples before subjecting them to pyrolysis (SU-P). The thermogravimetric analysis (TGA) curve of SU-P showed three distinct regions in the ranges of 30−300, 300−500, and 500−800 °C, and the three-stage regions of SU were in the ranges of 30−200 and 200−800 °C. The SU-P sample contains the sucrose−urea polymer, and during the first stage, highly volatile compounds such as water vapor are eliminated, leading to a weight loss of 11.0%. Medium volatile compounds like urea are eliminated during the second stage, creating a weight loss of 31.4%. Then, during the third stage, a weight loss of 20.1% was calculated due to the decomposition of the polymer's structure and the activated carbon produced. The total weight loss of SU-P during heating in a N_2 atmosphere was 62.5%. SU, which is already pyrolyzed, showed a weight loss of 9.6% during the first stage, which is less than what resulted with SU-P. This was due to the water molecules trapped in the carbon framework being low in number, since most of the water molecules have been eliminated during pyrolysis. Similarly, the weight loss obtained during the second stage was significantly low (0.9%), as most of the urea molecules were eliminated during pyrolysis. The weight loss that occurred during the third stage corresponds to the decomposition of the polymer and is 12.9%, which is less than that obtained with SU-P because most of the decomposition occurs during pyrolysis at 800 °C.

4.4. Textural Parameter Analysis. Textural parameters were analyzed by a BET surface area analyzer. Figure 5a shows the N_2 adsorption−desorption isotherms, and Figure 5b illustrates the Barrett−Joyner−Halenda (BJH) pore size distribution curves. Table 1 summarizes the textural parameters of the carbon−nitrogen adsorbents. Isotherms can be classified as type V, indicating the presence of mesopores. However, an extended hysteresis is present between the adsorption and desorption branches of the isotherm, deviating from the IUPAC classification and indicating that the pore structure may be changing as a function of amount adsorbed.[50]

The pore size distribution curves confirm that most of the pores are in the 15−100 nm range. Pores indicated by the BJH pore size distribution curves are produced during the polymerization of sucrose and urea, during pyrolysis when small molecules like CO_2, NH_3, and CH_4 escape and when the solid activating agents are washed and removed from the adsorbents after the pyrolysis.

https://doi.org/10.1021/acsomega.3c00339
ACS Omega 2023, 8, 16158−16173

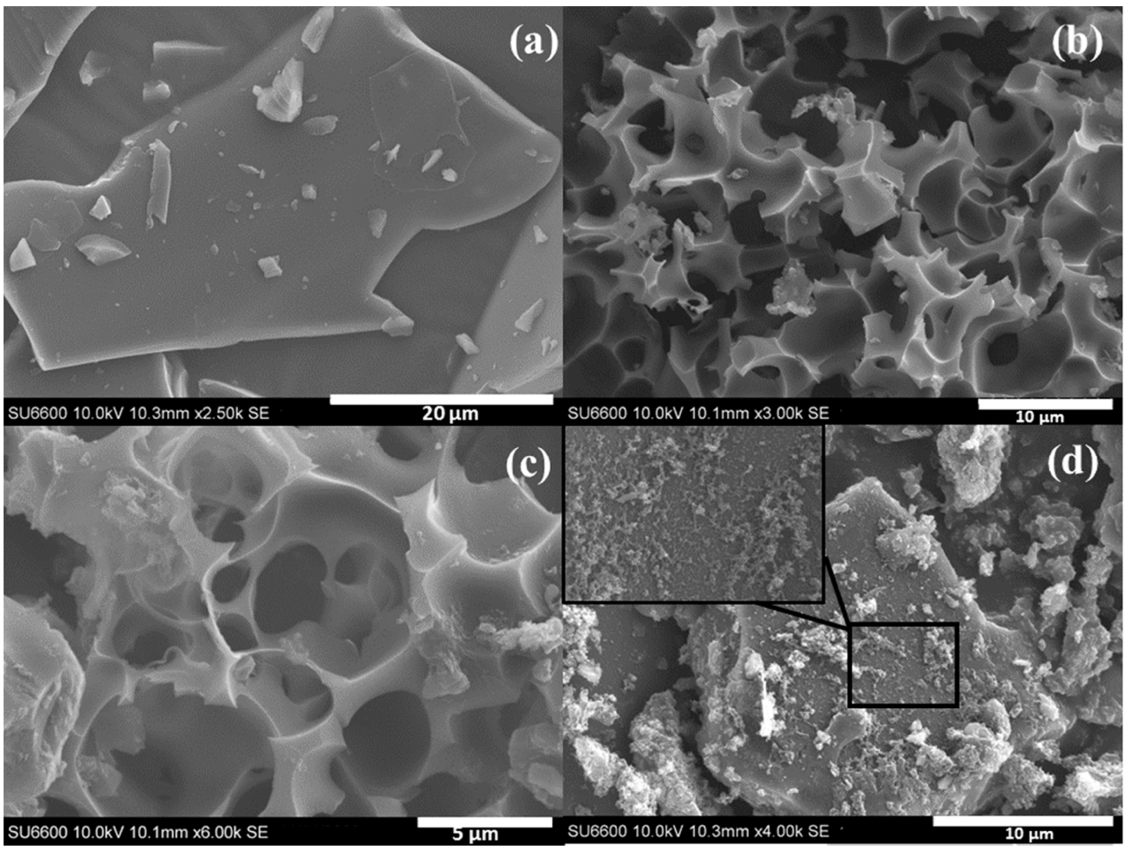

Figure 2. SEM images of (a) SU, (b, c) SU-KOH, and (d) SU-H_3PO_4; inset: high-magnification image of (d).

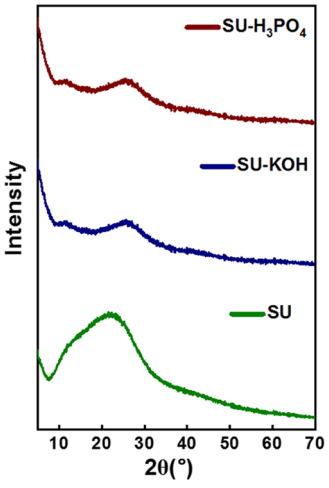

Figure 3. XRD patterns of SU, SU-KOH, and SU-H_3PO_4.

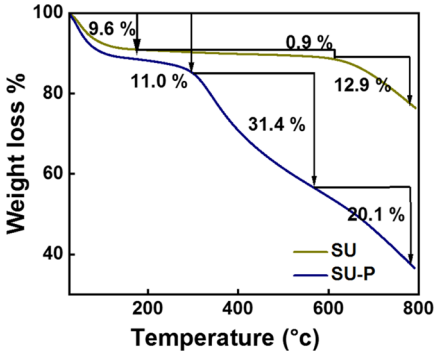

Figure 4. TGA curves of SU and SU-P.

As revealed by both the SEM and BET analyses, a significant porous structure will be formed when the solids (KOH) are used as activating agents because they create all three micropores, mesopores, and macropores upon washing the carbonized carbon adsorbents. The surface area of SU-KOH (282.02 m^2 g^{-1}) is higher than that of SU-H_3PO_4 (67.81 m^2 g^{-1}). SU revealed the smallest surface area (40.19 m^2 g^{-1}). The total pore volume also followed the same trend. The total pore volumes of SU-KOH, SU-H_3PO_4, and SU are 0.243, 0.136, and 0.04 cm^3 g^{-1}, respectively. These observations indicate that KOH as an activating agent has created more pores than H_3PO_4. It is evident that the porous structure of SU has not been significantly refined during polymerization and carbonization, leading to a smaller surface area. An improved porous system has been created as in SU-KOH and SU-H_3PO_4 only upon treatment with the activating agents.

4.5. Vibrational Spectroscopic Analysis. Fourier transform infrared (FT-IR) spectroscopy of SU and activated SU were collected to investigate functional groups present on the carbon surface (Figure 6a). The peak at 756 cm^{-1} is assigned to the C−H bending and the peak at 1157 cm^{-1} is attributed to C−O stretching. The peak at 1427 cm^{-1} represents the O−H bending present in alcohols. C═O stretching in lactams is represented by the peak at 1650 cm^{-1}, the peak at 1680 cm^{-1} shows the presence of C═O stretching present in secondary and tertiary amides, and the peak at 1740 cm^{-1} represents the C═O stretching in aldehyde and/or esters and/or lactones. The strong peak at 2360 cm^{-1} is attributed to O═C═O in CO_2 and is not related to the carbon adsorbent prepared. The

https://doi.org/10.1021/acsomega.3c00339
ACS Omega 2023, 8, 16158−16173

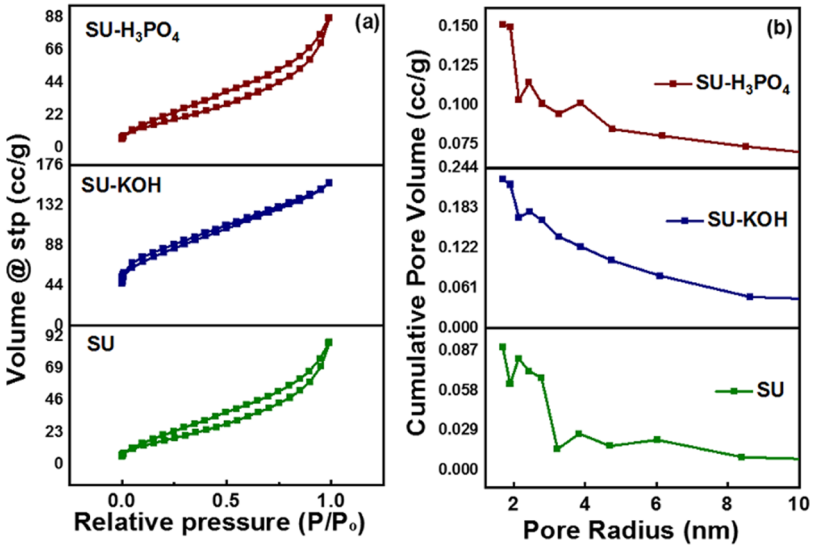

Figure 5. (a) Nitrogen adsorption−desorption isotherms and (b) BJH pore size distribution curves of SU, SU-KOH, and SU-H_3PO_4.

Table 1. Kinetics Parameters for MB Removal by SU-KOH and SU-H_3PO_4

		pseudo-first-order			pseudo-second-order		
sample	$Q_{e,exp}$ (g mg^{-1})	Q_e (g mg^{-1})	K_1 (min^{-1})	R^2	Q_e (g mg^{-1})	K_2 (mg g^{-1})	R^2
SU-KOH	384	411	0.039	0.77	361	2.33×10^{-6}	0.99
SU-H_3PO_4	108	108	132	0.95	82	7.3×10^{-7}	0.99

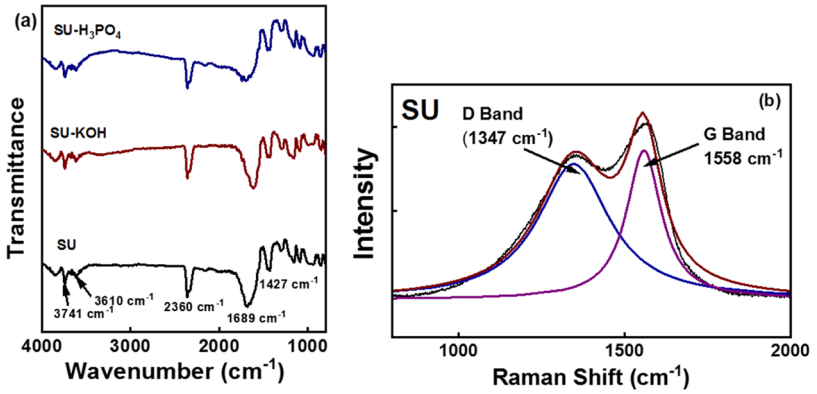

Figure 6. (a) FT-IR spectra of SU, SU-KOH, and SU-H_3PO_4. (b) Raman spectrum of SU.

peak at 2160 cm^{-1} is attributed to N═C═N stretching, while the peaks at 3610 and 3741 cm^{-1} are assigned to the O−H stretching in alcohols. The Raman spectrum of SU was obtained (Figure 6b). The D band at 1346.4 cm^{-1} is attributed to the breathing modes of sp^2 atoms in hexagons and the G band at 1557.9 cm^{-1} corresponds to the bond stretching of all pairs of sp^2 atoms in both rings and chains.[13,15] The intensity ratio of the D band to the G band is 0.90, indicating that the sp^2 atoms in hexagons are higher than those in both rings and chains, suggesting that SU is more amorphous.

4.6. XPS Analysis. XPS spectra were collected to study the chemical changes that occur at the surface following treatment with the activating agents. The higher-resolution spectrum of the C 1s of SU (Figure 7a) is deconvoluted into three peaks at 284.5, 285.9, and 287.8 eV, which correspond to the sp^2 hybridized C−C, C−O/C−N, and C═O bonds, respectively,[51] with relative abundance percentages of 60.61, 20.94, and 18.45%, respectively. The higher-resolution spectrum of the C 1s of SU-KOH (Figure 7b) also shows the same bonds in which the relative abundance of C−O has dramatically increased. The relative abundance percentages were 60.61, 20.94, and 18.45%, respectively. The higher-resolution spectrum of the C 1s of SU-KOH (Figure 7b) also shows the same bonds in which the relative abundance of C−O has dramatically increased. The relative abundance percentages of the same bonds are 38.78, 43.25, and 18.00%, respectively. Indicated here is that more oxygen-containing carbon-based functional groups have been created upon activation, since the activating agents oxidize the carbon surface in addition to what the porous system produces. The higher-resolution spectrum of the O 1s of SU is deconvoluted into three peaks at 530.5, 531.4, and 532.8 eV (Figure 7c), which are, respectively, attributed to C−OH, C−O, and C═O.[52] The same bonding nature in oxygen was observed in carbon activated with KOH (Figure 7d). The presence of N is confirmed by the XPS analysis. The higher-resolution spectrum of the N 1s of SU (Figure 7e) is deconvoluted into two peaks at 398.1 and 399.5 eV, which, respectively, correspond to pyridinic N (N6) and

https://doi.org/10.1021/acsomega.3c00339
ACS Omega 2023, 8, 16158−16173

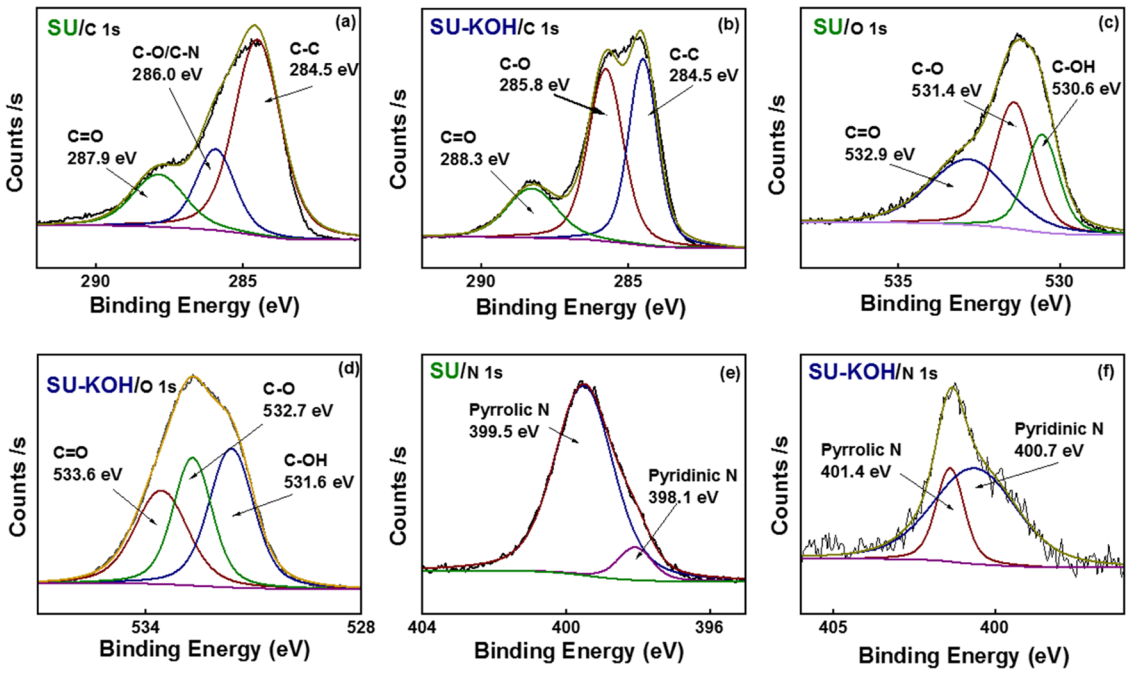

Figure 7. Higher-resolution spectra of C 1s of (a) SU and (b) SU-KOH, the higher-resolution spectra of O 1s of (c) SU and (d) SU-KOH, and the higher-resolution spectra of (e) SU and (f) SU-KOH.

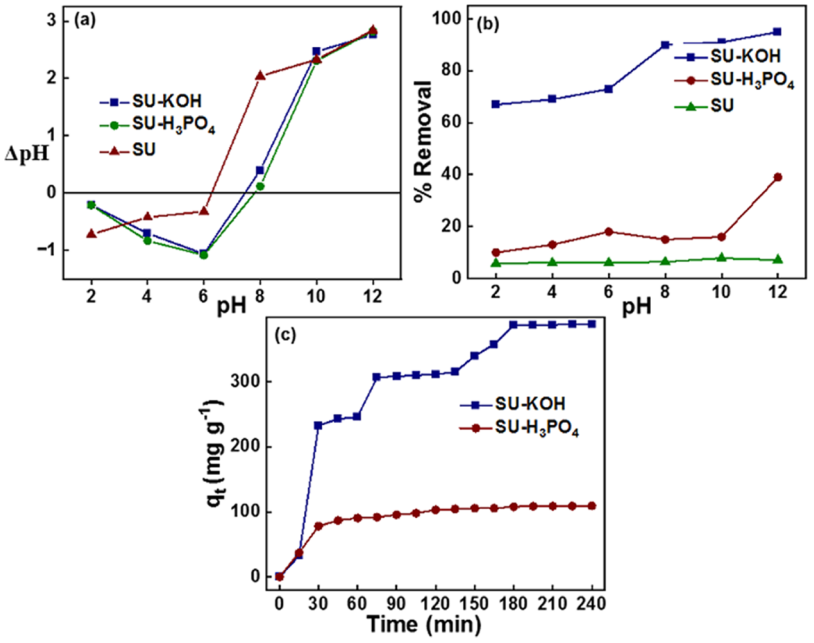

Figure 8. (a) Determination of the point of zero charge for the adsorbents. (b) Percentage removal versus the pH of SU, SU-KOH, and SU-H_3PO_4. (c) Variation in the adsorption capacity over time for SU-KOH and SU-H_3PO_4.

pyrrolic-N/pyridinic N (N-5).[30] Quantitative analysis shows that 90.87% of N is present as pyridinic N (N6) and only 9.13% of N is present as pyrrolic N/pyridinic N (N-5). The same chemical environment of N was observed in carbon activated by KOH (Figure 7f). However, there is an increase in the binding energy of N species, which is due to the abundantly present electronegative oxygen-containing functional groups after the activation. The C/N of SU is calculated to be 11:5. Sucrose was mixed with urea at a weight ratio of 1:1 where the C/N is also 1:1. The ratio has diminished due to the evaporation of urea during the polymerization and pyrolysis at high temperatures.

4.7. Effect of pH. The point of zero charge (PZC) of the adsorbents was evaluated to determine the surface charge of the adsorbents in each pH value (Figure 8a). It was observed that the PZC values of SU, SU-KOH, and SU-H_3PO_4 are 6.3, 7.5, and 7.8, respectively. The surface of the adsorbents is positively charged at a pH lower than the PZC, where negatively charged molecules would adsorb, and the surface is negatively charged at a pH higher than the PZC, in which the negatively charged molecules would adsorb. The effect of pH

https://doi.org/10.1021/acsomega.3c00339
ACS Omega 2023, 8, 16158−16173

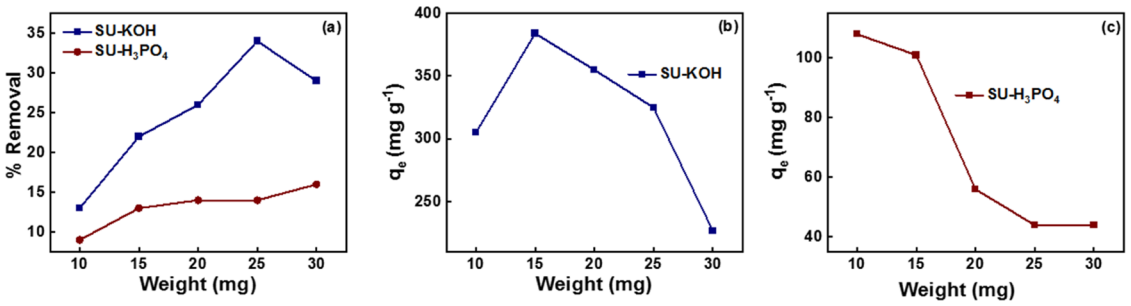

Figure 9. Variation of (a) the percentage removal of MB with respect to the weight of SU-KOH and SU-H_3PO_4, (b) adsorption capacity with respect to the weight of SU-KOH, and (c) adsorption capacity with respect to the weight of SU-H_3PO_4.

in removing MB using SU, SU-KOH, and SU-H_3PO_4 over a pH range of 2−12 was examined. The percentage of dye removal was calculated at each pH for all four adsorbents. As shown in Figure 8b, the percentage of MB removed by the adsorbents varied as SU-KOH > SU-H_3PO_4 > SU, where SU adsorbed a negligible amount of MB at all of the pH values. The percentage removal of MB by all three adsorbents was higher in alkaline pH values, which are greater than the respective PZC values because the surface of the adsorbents is negatively charged, hence facilitating the positively charged MB molecules. The adsorption capacity of all of the adsorbents increased with increasing pH, where the maximum adsorption capacity was found at 12, which is greater than the PZC of all three adsorbents. Adsorption capacities for adsorbing MB by SU-KOH, and SU-H_3PO_4 at pH 12 are 136.4 and 44 mg g^{-1}, respectively. MB is a cationic dye and a negative charge on the carbon surface will result in a higher adsorption ability. The total OH^- concentration increases with increasing pH, and hence, the total negative charge rendered on the carbon surface increases with increasing pH. This in turn enhances the electrostatic attractions between the positively charged MB and the negatively charged carbon surface, increasing the adsorption of MB. The formation of the dimeric form of MB at pH 12 greatly reduces the adsorption due to the inaccessibility of the dimeric form to the porous structure due to the steric hindrance. As the adsorption of MB by SU is negligible at all of the pH values, it was not considered for further analysis. This observation means that the presence of N in the carbon framework does not enhance the adsorption of MB despite N containing a lone pair electron. The surface activation and the textural properties only trigger the adsorption of MB to the adsorbents.

As revealed by the BET analysis, the surface area, total pore volume, and micropore volume of the activated adsorbents varied as SU-KOH > SU-H_3PO_4, reflecting the exact variation trend in the adsorption capacity (Figure 8c). Confirmed here is that the textural parameters play a major role in adsorbing MB to the carbon surface. As shown by both BET and SEM analyses, a well-developed hierarchical porous system was evident mainly in SU-KOH, where the porous system was not properly established in SU-H_3PO_4. MB molecules-containing adsorbate solution easily migrates through the channels formed in the hierarchical porous system due to the connection between macropores, mesopores, and micropores. The surface of the activated carbon is enriched with oxygen- and nitrogen-containing functional groups as discussed in the FT-IR and XPS analyses. Additionally, as revealed by the XPS analysis, the oxidation of the carbon surface by the activated reagents varied as KOH > H_3PO_4. Oxidation creates negatively charged oxygen-containing functional groups, which readily adsorb positively charged MB. Therefore, it is evident that the textural parameters including the surface area and the pore volume along with the surface-active sites created by the activating agents mainly govern the adsorption, and the contribution made by the nitrogen incorporated into the polymer by urea is negligible.

4.8. Variation of the Adsorbent Dosage. The effect of the adsorbent's weight on the adsorption of MB was studied with all three activated carbon materials by varying the weight of the adsorbent in the range of 10−30 mg in 5 mg increments. Concerning the adsorption kinetics, the weight of the adsorbent added to the MB solution varied in the 10−30 mg range in 5 mg increments in both SU-KOH and SU-H_3PO_4 materials where 50 mL of 200 and 500 ppm MB solutions were used, respectively.

A larger amount of dye molecules was adsorbed with increasing weight of the adsorbent dosage due to the presence of more active sites on the surface.

4.9. Adsorption Kinetics. The kinetics models were examined to understand the adsorption mechanism and dynamics. The initial dye adsorption rate by the activated carbon materials was high, as the empty adsorption sites are freely available for dye molecules to get adsorbed. The rate eventually slowed down and reached a plateau at 180 and 120 min in SU-KOH and SU-H_3PO_4, respectively, as the adsorption sites get saturated with prolonged dye adsorption. The adsorption capacity was calculated using eq 1, and the dye removal efficiency (R) was calculated by eq 2.

$$q_e = \frac{(C_0 - C_t)V}{m} \quad (1)$$

$$R = \frac{(C_0 - C_t)100\%}{C_0} \quad (2)$$

where q is the amount of MB adsorbed per unit mass of the adsorbent (mg g^{-1}), V is the volume of MB in L, m *is* the mass of the adsorbent in g, C_0 is the initial concentration of MB, and C_t is the concentration of MB at time t.

The highest adsorption capacities of SU-KOH and SU-H_3PO_4 are obtained with 15 and 10 mg, respectively, as shown in Figure 9b,c, respectively. The adsorption capacity of SU-KOH increased to 384 mg g^{-1} for 15 mg of the adsorbent from 108 mg g^{-1} with 10 mg of SU-KOH and decreased when the adsorbent dosage was further increased. The highest adsorption capacity of SU-H_3PO_4 (108 mg g^{-1}) was obtained with the lowest adsorbent dosage and declined when the adsorbent dose was increased. The percentage removals of MB by SU-KOH and SU-H_3PO_4 in different adsorbent dosages are

https://doi.org/10.1021/acsomega.3c00339
ACS Omega 2023, 8, 16158−16173

shown in Figure 9a. The amount of SU-KOH removed increased with a larger dosage of SU-KOH (up to 25 mg) where 34% of 500 ppm MB was removed in 180 min and fell to 29% with 30 mg of SU-KOH. This is due to the slowdown of the mass transport that occurred due to the coagulation of adsorbent particles at higher dosages, limiting the access of the adsorbate, MB, to the active sites of the adsorbent, SU-KOH. The percentage removed by SU-H_3PO_4 increased with an increasing adsorbent dosage where a maximum of 16% of 200 ppm MB was removed by 30 mg of SU-H_3PO_4. The number of active sites available in the increasing adsorbent weight resulted in more MB molecules being removed.

The pseudo-first-order and the pseudo-second-order kinetics models were built using the derived expressions given in eqs 3 and 4, respectively. The parameters of the expressions are defined as follows

$$\ln(q_e - q_t) = -kT + \ln(q_e) \quad (3)$$

$$\frac{t}{q_t} = \frac{t}{q_e} + \frac{1}{k_2 q_e^{\,2}} \quad (4)$$

where q_t is the amount of MB adsorbed at t time interval per unit mass of the adsorbent (mg g^{-1}), q_e is the amount of MB adsorbed at equilibrium per unit mass of the adsorbent (mg g^{-1}), k_1 is the adsorption rate constant for pseudo-first-order kinetics (1/min), k_2 is the adsorption rate constant for pseudo-second-order kinetics (g min^{-1}*mg^{-1}), and t is the time (min).

Additionally, $q_{e,cal}$ is the calculated amount of MB adsorbed at equilibrium per unit mass of the adsorbent (mg g^{-1}). All of the calculated kinetics parameters are tabulated in Table 2. The

Table 2. Kinetic Parameters of the Intraparticle Diffusion Model of SU-KOH

diffusion type	k_i (mg g^{-1}·min^{-1})	C (mg g^{-1})
bulk diffusion	124.8	−450.6
film diffusion	66.4	−268.3
pore diffusion	39.1	−140.3

pseudo-first-order kinetics models of SU-KOH and SU-H_3PO_4 are shown in Figure 10a,b, respectively, while the pseudo-second-order kinetic models of the adsorbents are exhibited in Figure 10c,d, respectively. The best-fitting kinetic model was selected depending on the linear correlation coefficient (R^2). That for the adsorption of MB to both SU-KOH and SU-H_3PO_4 of the pseudo-second-order model is 0.99 and those for the pseudo-first-order model are 0.77 and 0.95, respectively. It can be concluded that the adsorption of MB to the activated carbon materials follows the pseudo-second-order model, thus confirming the chemisorption of MB to the activated carbon materials.

The MB molecule is aromatic, and the electrons of the π bonds interact with the electrons of the π bonds of the aromatic rings present in the activated carbon materials forming $\pi-\pi$ interactions. Further, the negatively charged oxygen- and nitrogen-containing functional groups readily interact with the positively charged MB molecules, forming electrostatic interactions. The $q_{e,cal}$ values of all three materials match with the $q_{e,exp}$ values further, confirming that the MB molecules adsorb to the carbon surface following pseudo-second-order kinetics. The experimental adsorption capacities of SU-KOH and SU-H_3PO_4 are 384 and 108 mg g^{-1}, respectively. As discussed in the pH section, the surface-active sites created during the activation of the surface area and the pore volume also contributed to the resulting variation. Kinetic data were further fitted to the intraparticle diffusion model according to the expression given in eq 5.

$$q_t = k_i t^{1/2} + C \quad (5)$$

where k_i is the diffusion rate constant, C is the intercept, and t is the time in min.

The intraparticle diffusion models of SU-KOH and SU-H_3PO_4 are shown in Figure 10e,f, respectively. According to Figure 10e, it is evident that the kinetics of the adsorption of MB to SU-KOH consist of three consecutive stages, i.e., bulk diffusion, film diffusion, and pore diffusion. More specifically, the first phase observed at $3.8 < t_{1/2} < 5.4$ min represents the surface and intraparticle diffusion process with a diffusion constant of 124.8 mg g·min^{-1}, and the thickness of the boundary layer is −450.6 mg g^{-1}. The thickness is negative, suggesting that the sorption is negative and spontaneous. The second phase resulted in the range of $7.7 < t_{1/2} < 8.7$, representing the liquid film diffusion, while the third phase obtained at $11.6 < t_{1/2} < 13.4$ represents the diffusion of MB dye molecules through the pores to the active sites of SU-KOH. The k_i and C values for the adsorption of MB to each activated carbon material are tabulated in Table 2. The rate of bulk diffusion is the highest, and the rate of film diffusion is greater than the rate of pore diffusion in the SU-KOH system. The thickness of the boundary layer decreased when the diffusion mechanism changed from bulk to film and to pore diffusion. However, being different from the adsorption of MB to SU-KOH, the adsorption of MB to SU-H_3PO_4 does not show three stages and the rate of adsorption increased gradually. This observation is consistent with the observation made with the adsorption of MB to SU-H_3PO_4; although the adsorption capacity is comparatively lower in the SU-H_3PO_4 system, the rate of adsorption was high.

4.10. Adsorption Isotherms. The effect of MB concentration on the removal of MB by SU-KOH and SU-H_3PO_4 was studied by varying the MB concentration in the ranges of 100−500 and 25−200 ppm, respectively. The adsorbent dosage was kept constant at 10 and 10 mg, respectively, and 50 mL was used for the study. The variation in adsorption capacity and the percentage of MB removed with respect to the concentration of MB of SU-KOH and SU-H_3PO_4 are shown in Figure 11a,c, respectively. Meanwhile, the efficiency of dye removal by both activated carbon adsorbents is reported in Figure 11b,d, respectively. The adsorption capacity increased with increasing concentration of MB, where the highest adsorption capacity of SU-KOH (384 mg g^{-1}) is obtained with 500 ppm MB, while that of SU-H_3PO_4 (108 mg g^{-1}) resulted with a 200 ppm MB solution. The concentration gradient established between the MB solution and the adsorbent surface increased with increasing concentration of MB. However, the dye removal efficiency decreased with increasing MB concentration. The highest removal efficiency of 34% was obtained with 100 ppm MB, which fell to 21% with 500 ppm MB using SU-KOH. Similarly, the largest amount of dye removal (20%) resulted when 25 ppm MB was used, and the lowest percentage of dye removal (10%) was obtained with a 200 ppm MB solution.

Adsorption data were fitted to four different isotherm models: Langmuir, Freundlich, Temkin, and Dubinin−Radushkevich. The Langmuir adsorption isotherm model

https://doi.org/10.1021/acsomega.3c00339
ACS Omega 2023, 8, 16158−16173

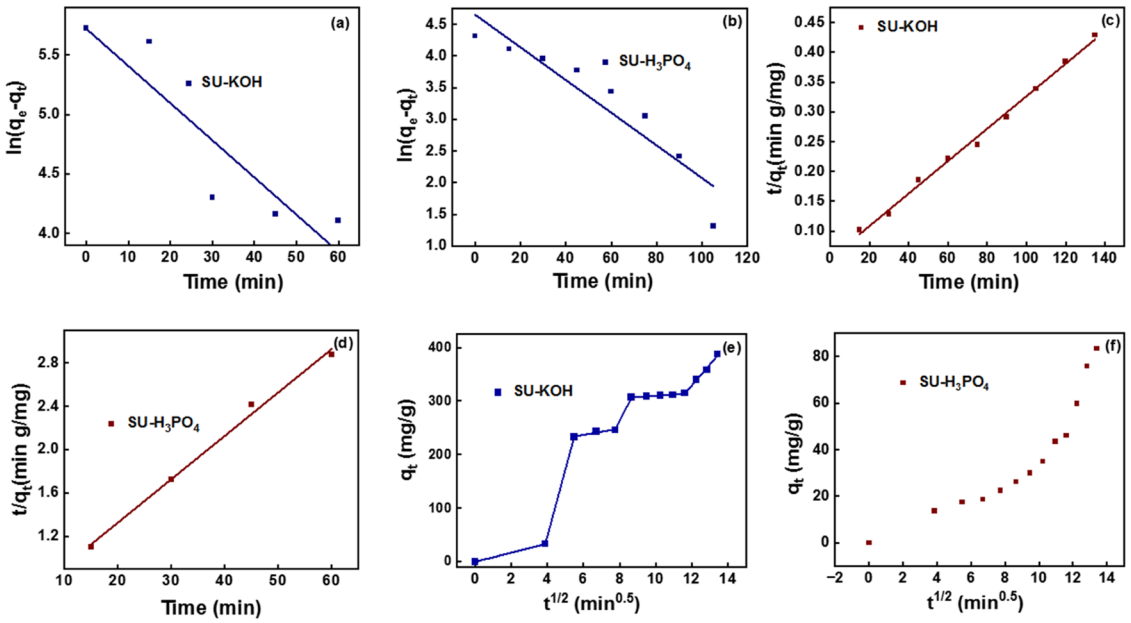

Figure 10. Pseudo-first-order kinetic model of (a) SU-KOH and (b) SU-H_3PO_4, the pseudo-first-order kinetic model of (c) SU-KOH and (d) SU-H_3PO_4, and the intraparticle diffusion models (e) SU-KOH and (f) SU-H_3PO_4.

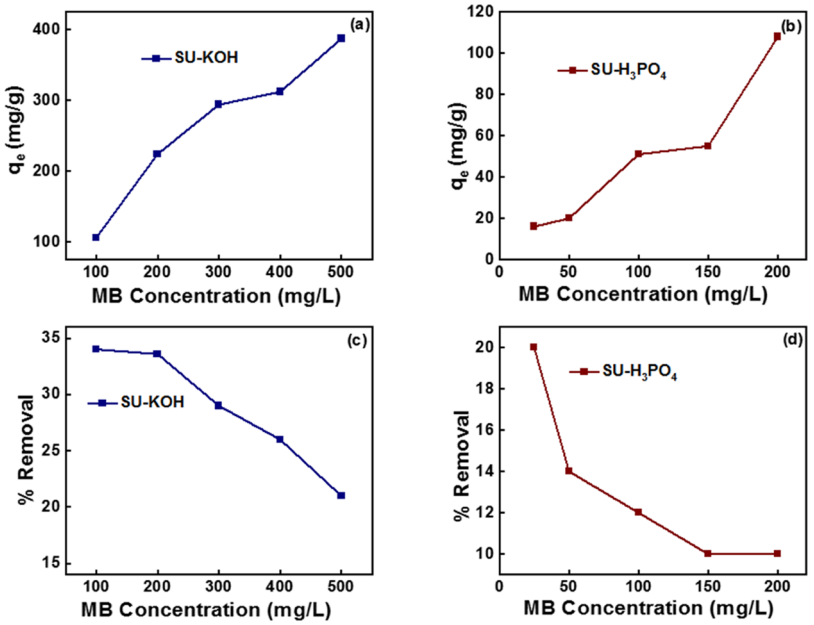

Figure 11. Variation in the adsorption capacity of (a) SU-KOH and (b) SU-H_3PO_4 and the variation in the removal of MB by (c) SU-KOH and (d) SU-H_3PO_4 with respect to the concentration of MB.

assumes the monolayer adsorption of adsorbates to homogeneous adsorbate surfaces containing definite localized sites. Further, the model assumes uniform energies of adsorption to the surface with no lateral interactions and no steric hindrance between the adsorbates. The Langmuir isotherm model can be represented by eq 6.

$$\frac{1}{q_e} = \frac{1}{q_m K_L C_e} + \frac{1}{q_m} \tag{6}$$

where C_e is the equilibrium concentration of the adsorbate (mg L^{-1}), q_e is the amount of adsorbed (adsorbate) at equilibrium per unit mass of the adsorbent (mg g^{-1}), K_L is the Langmuir constant related to adsorption capacity (L mg^{-1}), and q_m is the practical limiting adsorption capacity (mg g^{-1}).

The q_m and K_L values are calculated from the slope and the intercept of a plot constructed between C_e/q_e versus C_e, as shown in Figure 12a,b. These correspond to the Langmuir isotherms of SU-KOH and SU-H_3PO_4, respectively.

The Freundlich isotherm assumes that adsorbates adsorb to a heterogeneous surface and describe the nonideal reversible adsorption process. The linear form of the Freundlich isotherm model is given in eq 7.

$$\ln(q_e) = \ln\left(K_f + \frac{1}{n}\ln(C_e)\right) \tag{7}$$

https://doi.org/10.1021/acsomega.3c00339
ACS Omega 2023, 8, 16158−16173

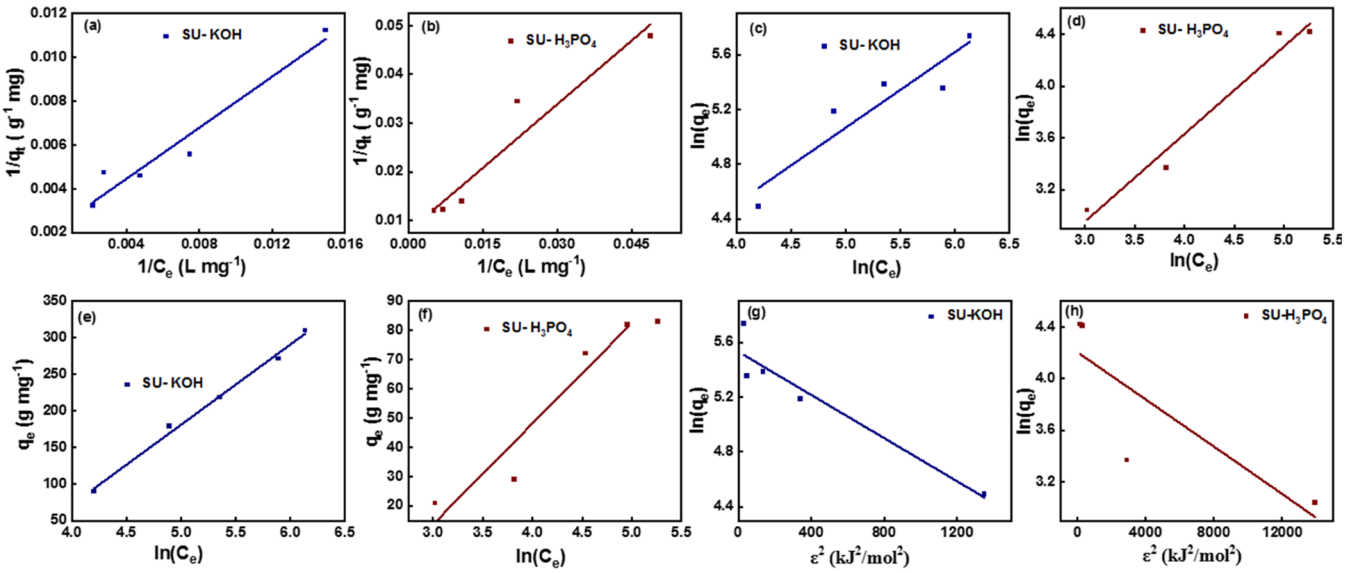

Figure 12. Langmuir isotherms of (a) SU-KOH and (b) SU-H_3PO_4, Freundlich isotherms of (c) SU-KOH and (d) SU-H_3PO_4, Temkin isotherms of (e) SU-KOH and (f) SU-H_3PO_4, and Dubinin isotherms of (g) SU-KOH and (h) SU-H_3PO_4.

Table 3. Isotherm Parameters of Langmuir, Freundlich, Temkin, and Dubinin Isotherm Models for MB Removal by SU-KOH and SU-H_3PO_4

	Langmuir		Freundlich		Temkin		Dubinin	
sample	K_L (L mg^{-1})	R^2	K_f (L g^{-1})	R^2	K_T (L mg^{-1})	R^2	K_D (mol^2 kJ^{-2})	R^2
SU-KOH	4.1×10^{-3}	0.93	18.17	0.83	3.2×10^{-2}	0.99	9.2×10^{-4}	0.87
SU-H_3PO_4	7.6×10^{-2}	0.90	3.65	0.95	6.0×10^{-2}	0.90	1.4×10^{-4}	0.56

where q_e is the amount of adsorbed (adsorbate) at equilibrium per unit mass of the adsorbent (mg g^{-1}), C_e is the equilibrium concentration of the adsorbate (mg L^{-1}), K_F is the Freundlich adsorption capacity (mg g^{-1}), and $1/n$ is the adsorption intensity.

The values of n and K_F can be calculated by the slope and the intercept of the plot of log q_e versus log C_e, respectively. The Freundlich isotherms of SU-KOH and SU-H_3PO_4 are shown in Figure 12c,d, respectively.

The Temkin isotherm model considers the effects of indirect adsorbent/adsorbate interactions on the adsorption process. It also assumes that the heat of adsorption of all molecules in the layer would decrease linearly as a result of an increase in surface coverage. The linear form of the Temkin isotherm model is given in eq 8.

$$q_e = B \ln(C_e) + B \ln(K_T) \tag{8}$$

where q_e is the amount of adsorbed (adsorbate) at equilibrium per unit mass of the adsorbent (mg g^{-1}), C_e is the equilibrium concentration of the adsorbate (mg L^{-1}), R is the universal gas constant (J mol^{-1} K^{-1}), T is the absolute temperature (K)q. K_T is the Temkin isotherm constant (L g^{-1}), and b is the Temkin constant, which is related to heat (J mol^{-1}).

The values of b and K_T can be calculated from the slope and intercept of the plot constructed q_e versus ln C_e. The Temkin isotherms of SU-KOH and SU-H_3PO_4 are shown in Figure 12e,f, respectively.

The Dubinin−Radushkevich isotherm model was developed to determine the effect of the porosity of the adsorbents in which the adsorption process was related to micropore filling compared to the layer-by-layer adsorption on pore walls.[53,54] The linear form of the Temkin isotherm model is given in eqs 9 and 10.

$$\ln(q_e) = \ln(q_m) - K_d\varepsilon^2 \tag{9}$$

$$\varepsilon = RT \ln(1 + 1/C_e) \tag{10}$$

where q_e is the amount of adsorbed (adsorbate) at equilibrium per unit mass of the adsorbent (mg g^{-1}). C_e is the equilibrium concentration of the adsorbate (mg L^{-1}), R is the universal gas constant (J mol^{-1} K^{-1}), T is the absolute temperature (K), K_d is the Dubinin constant (mol^2 kJ^{-2}), and ε is the potential energy (kJ mol^{-1}).

The parameters calculated from the isotherm models are tabulated in Table 3. The best-fitting model was determined by considering the correlation coefficient (R^2) values. The SU-KOH adsorbent followed the Temkin isotherm model with an R^2 of 0.9939, and SU-H_3PO_4 followed the Freundlich isotherm model with an R^2 of 0.9546. The monolayer adsorption values determined using the Langmuir isotherm model were 469 and 129 mg g^{-1} for SU-KOH and SU-H_3PO_4, respectively, and they agree with the value obtained from the experimental data: 387 and 108 mg g^{-1}. The adsorption feasibility is calculated by eq 11.

$$R_l = \frac{1}{1 + K_L C_0} \tag{11}$$

where K_L is the Langmuir constant in mg L^{-1} and C_0 is the initial MB concentration in mg L^{-1}.

The R_L value denotes the type of isotherm: favorable ($0 < R_L < 1$), irreversible ($R_L = 0$), unfavorable ($R_L > 1$), and linear ($R_L = 1$). R_L values determined for the adsorption of MB to SU-

https://doi.org/10.1021/acsomega.3c00339
ACS Omega 2023, 8, 16158−16173

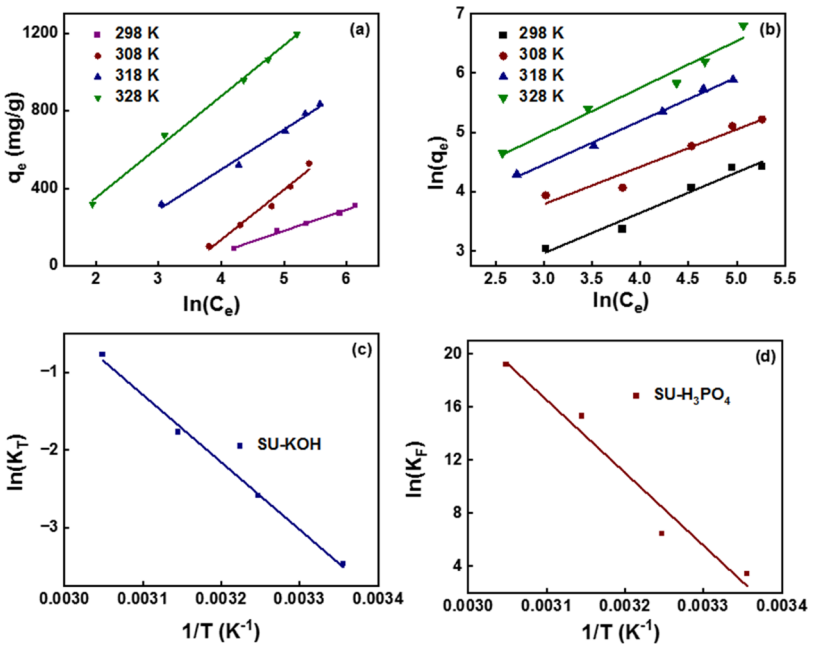

Figure 13. Temkin isotherms plotted for the adsorption of MB to (a) SU-KOH, Freundlich isotherms plotted for the adsorption of MB to (b) SU-H_3PO_4 in four different temperatures, and van't Hoff plots of (c) SU-KOH (d) SU-H_3PO_4.

Table 4. Kinetic Parameters Calculated at Different Temperatures

	equilibrium rate constant (K)		pseudo-second-order rate constant (k_2)/mg g^{-1}	
temperature (K)	SU-KOH (K_T)/L mg^{-1}	SU-H_3PO_4 (K_F)/L g^{-1}	SU-KOH	SU-H_3PO_4
298	3.12×10^{-2}	3.11×10^{1}	2.33×10^{-6}	7.32×10^{-7}
308	7.51×10^{-2}	6.26×10^{2}	1.11×10^{-4}	1.75×10^{-4}
318	1.71×10^{-1}	4.55×10^{6}	2.74×10^{-4}	2.31×10^{-3}
328	4.62×10^{-1}	2.18×10^{8}	6.76×10^{-4}	2.68×10^{-3}

KOH and SU-H_3PO_4 are 0.0037 and 0.0089, respectively, and indicate favorable adsorption.

4.11. Adsorption Thermodynamics. The thermodynamics of adsorption of MB onto SU-KOH and SU-H_3PO_4 was studied by varying the concentration of MB as described in Section 2.2.6 at four different temperatures, i.e., 25, 35, 45, and 55 °C. The obtained data were fitted to the Temkin and Freundlich isotherms for SU-KOH and SU-H_3PO_4, respectively (see Figure 13a,b), to calculate the respective equilibrium rate constants at each temperature that are needed to plot the van't Hoff plots, as shown in Figure 13c,d, respectively. The equilibrium rate constants of both isotherm models increased with increasing temperature (Table 4). Temkin and Freundlich isotherm models were selected to be consistent with the conclusion asserted in Section 4.10.

The thermodynamic parameters, change in enthalpy (ΔH°), change in entropy (ΔS°), and change in Gibbs free energy (ΔG°) were calculated for the adsorption of MB using eqs 12 and 13.

$$\ln K = \frac{\Delta H}{RT} + \frac{\Delta S}{R} \tag{12}$$

$$\Delta G = \Delta H - T\Delta S \tag{13}$$

where R is the universal gas constant (8.314 J mol^{-1} K^{-1}), T is the temperature in K, and K is the equilibrium constant.

The changes in entropy and enthalpy were determined from van't Hoff plots of ln(K_L) versus $1/T$, as shown in Figure 13c,d for SU-KOH and SU-H_3PO_4, respectively. All of the thermodynamic parameters are tabulated in Table 5.

Table 5. Thermodynamic Parameters Calculated for the Adsorption of MB to SU-KOH and SU-H_3PO_4

parameter		SU-KOH	SU-H_3PO_4
activation energy (kJ mol^{-1})		+92.4	+133.6
enthalpy (kJ mol^{-1})		+65.5	+32.4
entropy (J mol^{-1} K^{-1})		+223.6	+112.8
Gibbs free energy (kJ mol^{-1})	298 K	−1.13	−1.21
	308 K	−3.37	−2.34
	318 K	−5.60	−3.47
	328 K	−7.84	−4.26

Adsorption capacity values obtained at different temperatures are summarized in Table 6.

Table 6. Variation of Adsorption Capacity with Temperature

	Q_e (mg g^{-1})	
temperature (K)	SU-KOH	SU-H_3PO_4
298	387	108
308	528	184
318	835	361
328	1268	897

https://doi.org/10.1021/acsomega.3c00339
ACS Omega 2023, 8, 16158−16173

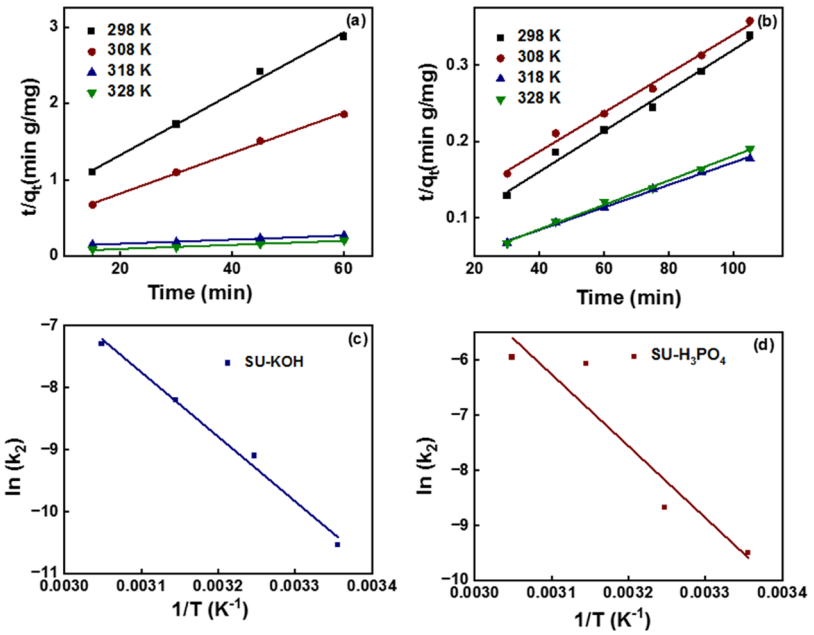

Figure 14. Pseudo-second-order kinetic model plotted the adsorption of MB at four different temperatures to (a) SU-KOH and (b) SU-H_3PO_4, and the Arrhenius plots constructed for the adsorption of (c) SU-KOH and (d) SU-H_3PO_4.

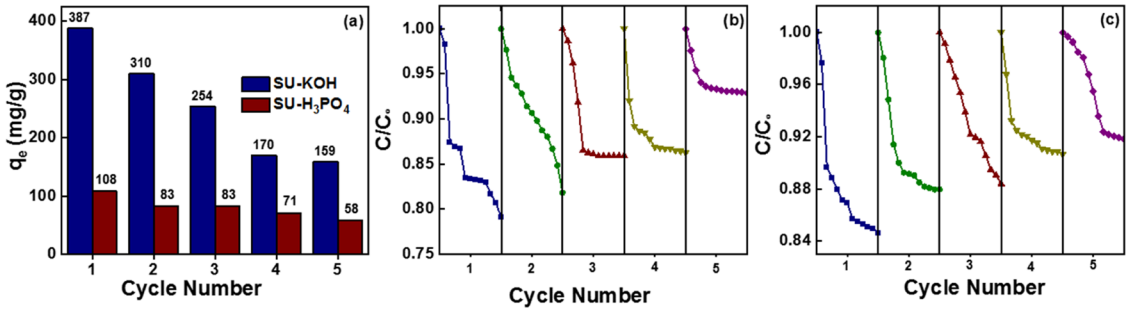

Figure 15. (a) Variation of adsorption capacity with the cycle numbers of SU-KOH and SU-H_3PO_4, and variation of C/C_o with the cycle numbers of (b) SU-KOH and (c) SU-H_3PO_4.

The adsorption capacity improved with increasing temperature in which the maximum adsorption capacity was obtained at 55 °C for SU-KOH and SU-H_3PO_4 as 1268 and 897 mg g^{-1}, respectively, where the adsorption capacity of SU-KOH is 1.4 times greater than that of SU-H_3PO_4, which was 3.6 times at 25 °C. Further, the adsorption capacity of SU-KOH increased by 3.3-fold and that of SU-H_3PO_4 by 8.3 times when the temperature increased from 25 to 55 °C. Therefore, it is evident that the increase in the temperature has greatly affected the adsorption of MB to SU-H_3PO_4 compared to SU-KOH. Further, it could be concluded that the adsorption of MB to the activated materials is endothermic where the change in the Gibbs free energy (ΔG) increased with increasing temperature. ΔG being negative at all of the temperatures shows that the MB adsorption to the adsorption materials is spontaneous in nature and feasible.

The pseudo-second-order kinetic graphs were plotted at four different temperatures for the adsorption of MB to SU-KOH and SU-H_3PO_4 (Figure 14a,b, respectively) to calculate the pseudo-second-order rate constants required to construct the Arrhenius plots shown in Figure 14c,d, respectively. The rate constants increased with increasing temperature, as shown in Table 4. The Arrhenius equation is represented in eq 14.

$$\ln(K) = -\frac{E_a}{RT} + \ln(A) \tag{14}$$

where k is the rate constant, A is the pre-exponential factor, E_a is the activation energy, R is the universal gas constant, and T is the absolute temperature.

The activation energies for the adsorption of MB to SU-KOH and SU-H_3PO_4 calculated from the slope of the plots are +92.4 and +133.6 kJ mol^{-1}, respectively. The pre-exponential factors calculated for SU-KOH and SU-H_3PO_4 are 4.23×10^{10} and A_E 5.9×10^{14}, respectively.

4.12. Reusability Study. The reusability of an adsorbent is an important parameter to especially evaluate the suitability of the adsorbent to industry. Variation in the adsorption capacity of both activated carbon materials with respect to the cycle number is shown in Figure 15a, while the variation of the C/C_o of MB adsorption to SU-KOH and SU-H_3PO_4 are given in Figure 15b,c, respectively. The adsorption capacity of SU-KOH declined from 387 mg g^{-1} (first cycle) to 159 mg g^{-1} in the fifth cycle and that of SU-H_3PO_4 dropped from 108 mg g^{-1} (first cycle) to 58 mg g^{-1} in the fifth cycle. The percentage reduction in the adsorption capacity of SU-KOH (58.9%) is greater than that of SU-H_3PO_4 (46.3%). The reduction in the adsorption capacity in both carbon materials could be due to

https://doi.org/10.1021/acsomega.3c00339
ACS Omega 2023, 8, 16158−16173

Table 7. Comparison of MB Removal by Carbon Activated by KOH and H_3PO_4 Derived from Other Sources

KOH			H_3PO_4		
adsorbent	Q_e (mg g^{-1})	reference	adsorbent	Q_e (mg g^{-1})	reference
sucrose−urea	1268	[the present study]	sucrose−urea	897	[the present study]
wheat straw	146.8	55	rice husks	578.0	56
peanut hulls	388.5	57	peanut hulls	42.2	57
coconut leaves	151.5	58	carpet waste-activated carbon	699.3	59
dragon fruit peel	195.2	60	tea waste	238.1	61
sugarcane bagasse waste	136.5	62	mangosteen peel	163.6	63
coffee husk	357.4	64	watermelon rind	284	65
bamboo chip	305.3	66	grass	241.3	67
Egyptian agricultural waste	333	68	corn stigma fiber	330.5	69

the pore obstruction caused by the coagulation of MB molecules. Further, the active sites are saturated with chemisorbed MB molecules because they do not get washed off when the materials are washed with distilled water and ethanol. Moreover, as the weight of the adsorbent used is very small (SU-KOH—15 mg) and (SU-H_3PO_4—10 mg), there could be a loss of the adsorbent during constant washing, thus further leading to a reduction in adsorption.

Adsorption capacities obtained in this study were compared with other carbon materials from different sources, which in the literature were activated by KOH and H_3PO_4 (Table 7). The adsorption capacity of SU-KOH is higher than that of the carbon derived from other sources, which were also activated by KOH. Similarly, the adsorption capacity of SU-H_3PO_4 was higher than that of carbon materials originating from other raw materials, which were activated by H_3PO_4. Based on our findings, we could not detect any carbon-related source activated by KOH and H_3PO_4 showing a higher adsorption capacity than what we obtained in this study (1268 and 897 mg g^{-1}, respectively).

5. CONCLUSIONS

Nitrogen-enriched carbon materials were successfully synthesized by pyrolyzing the sucrose−urea polymer at 800 °C. A hierarchically porous system was devised after removing the activating agents KOH and H_3PO_4 from the activated carbon. The best pH level for the adsorption of MB to both activated adsorbents is 12. Adsorption capacity enhanced with increasing concentration of MB but fell with increasing adsorbent dosage. The maximum adsorption capacity of SU-KOH was 1.4 times higher than that of H_3PO_4 due to the high surface area, high total pore volume, and large number of surface functional groups created during the activation. Adsorption of MB followed pseudo-second-order kinetics, indicating the chemisorption of MB to the adsorbents. The best-fitted isotherm models for the adsorption of MB to SU-KOH and SU-H_3PO_4 are the Temkin and Freundlich variants, respectively. Both the activated adsorbents were effective in removing MB for consecutive five cycles with some activity loss after each cycle. An increase in the adsorption of MB with increasing temperature suggests endothermic adsorption of MB to both SU-KOH and SU-H_3PO_4. The nitrogen-enriched carbon materials activated by KOH and H_3PO_4 show potential in treating wastewater contaminated by methylene blue economically and efficiently.

ASSOCIATED CONTENT

Supporting Information

The Supporting Information is available free of charge at https://pubs.acs.org/doi/10.1021/acsomega.3c00339.

Nonlinear models of kinetics and isotherms showing adsorption of MB to adsorbents (PDF)

AUTHOR INFORMATION

Corresponding Author

Charitha Thambiliyagodage − *Faculty of Humanities and Sciences, Sri Lanka Institute of Information Technology, Malabe 10115, Sri Lanka;* orcid.org/0000-0003-0906-4441; Email: charitha.t@sliit.lk

Authors

Heshan Liyanaarachchi − *Faculty of Humanities and Sciences, Sri Lanka Institute of Information Technology, Malabe 10115, Sri Lanka*

Hasindhi Lokuge − *College of Chemical Sciences, Institute of Chemistry Ceylon, Rajagiriya, CO 10107, Sri Lanka*

Saravanamuthu Vigneswaran − *Faculty of Engineering and Information Technology, University of Technology Sydney, Broadway, NSW 2007, Australia; Faculty of Sciences & Technology (RealTek), Norwegian University of Life Sciences, Ås N-1432, Norway*

Complete contact information is available at: https://pubs.acs.org/10.1021/acsomega.3c00339

Funding

This research was supported by the Accelerating Higher Education Expansion and Development (AHEAD) Operation of the Ministry of Higher Education funded by the World Bank.

Notes

The authors declare no competing financial interest.

ACKNOWLEDGMENTS

The authors acknowledge the Sri Lanka Institute of Nanotechnology for providing the instrument facilities.

REFERENCES

(1) Al-Tohamy, R.; Ali, S. S.; Li, F.; Okasha, K. M.; Mahmoud, Y. A. G.; Elsamahy, T.; Jiao, H.; Fu, Y.; Sun, J. A Critical Review on the Treatment of Dye-Containing Wastewater: Ecotoxicological and Health Concerns of Textile Dyes and Possible Remediation Approaches for Environmental Safety. *Ecotoxicol. Environ. Saf.* **2022**, *231*, No. 113160.

(2) Thambiliyagodage, C. Efficient Photocatalysis of Carbon Coupled TiO2 to Degrade Pollutants in Wastewater—A Review. *Environ. Nanotechnol., Monit. Manage.* **2022**, *18*, No. 100737.
(3) Rashid, R.; Shafiq, I.; Akhter, P.; Iqbal, M. J.; Hussain, M. A State-of-the-Art Review on Wastewater Treatment Techniques: The Effectiveness of Adsorption Method. *Environ. Sci. Pollut. Res.* **2021**, *28*, 9050−9066.
(4) Thambiliyagodage, C. Activity Enhanced TiO2 Nanomaterials for Photodegradation of Dyes—A Review. *Environ. Nanotechnol., Monit. Manage.* **2021**, *16*, No. 100592.
(5) Gita, S.; Shukla, S. P.; Saharan, N.; Prakash, C.; Deshmukhe, G. Toxic Effects of Selected Textile Dyes on Elemental Composition, Photosynthetic Pigments, Protein Content and Growth of a Freshwater Chlorophycean Alga Chlorella Vulgaris. *Bull. Environ. Contam. Toxicol.* **2019**, *102*, 795−801.
(6) Berradi, M.; Hsissou, R.; Khudhair, M.; Assouag, M.; Cherkaoui, O.; El Bachiri, A.; El Harfi, A. Textile Finishing Dyes and Their Impact on Aquatic Environs. *Heliyon* **2019**, *5*, No. e02711.
(7) Moradihamedani, P. Recent Advances in Dye Removal from Wastewater by Membrane Technology: A Review. *Polym. Bull.* **2021**, *79*, 2603−2631.
(8) Yang, X.; You, F.; Zhao, Y.; Bai, Y.; Shao, L. Confinedly Assembling Surface Nanocoating to Manipulate Nanofiltration Membranes for Highly-Efficient Dye Removal. *ES Energy Environ.* **2018**, *1*, 106−113.
(9) Thambiliyagodage, C.; Ranchagoda, S.; Mirihana, S. In *A Comparison Study of Removing Rhodamine B from Wastewater by Nitric Acid Functionalized Rice Husk, Coconut Husk and Synthetic Porous Carbon*, ICSBE 2020: Proceedings of the 11th International Conference on Sustainable Built Environment, Springer, 2022; pp 587−602.
(10) Sharma, R.; Malaviya, P. Constructed Wetlands for Textile Wastewater Remediation: A Review on Concept, Pollutant Removal Mechanisms, and Integrated Technologies for Efficiency Enhancement. *Chemosphere* **2022**, *290*, No. 133358.
(11) Ghuge, S. P.; Saroha, A. K. Catalytic Ozonation of Dye Industry Effluent Using Mesoporous Bimetallic Ru-Cu/SBA-15 Catalyst. *Process Saf. Environ. Prot.* **2018**, *118*, 125−132.
(12) Usgodaarachchi, L.; Thambiliyagodage, C.; Wijesekera, R.; Vigneswaran, S.; Kandanapitiye, M. Fabrication of TiO2 Spheres and a Visible Light Active α-Fe2O3/TiO2-Rutile/TiO2-Anatase Heterogeneous Photocatalyst from Natural Ilmenite. *ACS Omega* **2022**, *7*, 27617−27637.
(13) Thambiliyagodage, C.; Usgodaarachchi, L.; Jayanetti, M.; Liyanaarachchi, C.; Kandanapitiye, M.; Vigneswaran, S. Efficient Visible-Light Photocatalysis and Antibacterial Activity of TiO2-Fe3C-Fe-Fe3O4/Graphitic Carbon Composites Fabricated by Catalytic Graphitization of Sucrose Using Natural Ilmenite. *ACS Omega* **2022**, *7*, No. 25403.
(14) Ikram, M.; Haider, A.; Naz, S.; Bari, M. A.; Haider, J.; Ul-Hamid, A.; Nabgan, W.; Imran, M.; Nazir, G.; Ali, S. Chitosan and Carbon Nitride Doped Barium Hydroxide Nanoparticles Served as Dye Degrader and Bactericidal Potential: A Molecular Docking Study. *Int. J. Biol. Macromol.* **2023**, *224*, 938−949.
(15) Thambiliyagodage, C.; Hakat, Y.; Bakker, M. One Pot Synthesis of Carbon/Ni Nanoparticle Monolithic Composites by Nanocasting and Their Catalytic Activity for 4-Nitrophenol Reduction. *Curr. Catal.* **2006**, *5*, 135−146.
(16) Sivarajasekar, N.; Baskar, R. Agriculture Waste Biomass Valorisation for Cationic Dyes Sequestration:A Concise Review. *J. Chem. Pharm. Res.* **2015**, *7*, 737−748.
(17) Usgodaarachchi, L.; Thambiliyagodage, C.; Wijesekera, R.; Bakker, M. G. Synthesis of Mesoporous Silica Nanoparticles Derived from Rice Husk and Surface-Controlled Amine Functionalization for Efficient Adsorption of Methylene Blue from Aqueous Solution. *Curr. Res. Green Sustainable Chem.* **2021**, *4*, No. 100116.
(18) Gunathilaka, H.; Thambiliyagodage, C.; Usgodaarchchi, L.; Angappan, S. In *Effect of Surfactants on Morphology and Textural Parameters of Silica Nanoparticles Derived from Paddy Husk and Their Efficient Removal of Methylene Blue*, Proceedings of the International Conference on Innovations in Energy Engineering & Cleaner Production (IEECP'21), San Francisco, CA, USA, 2021.
(19) Rashid, J.; Azam, R.; Kumar, R.; Ahmad, M.; Rehman, A.; Barakat, M. A. Sulfonated Polyether Sulfone Reinforced Multiwall Carbon Nanotubes Composite for the Removal of Lead in Wastewater. *Appl. Nanosci.* **2019**, *9*, 1695−1705.
(20) Liu, S.; Ge, H.; Wang, C.; Zou, Y.; Liu, J. Agricultural Waste/Graphene Oxide 3D Bio-Adsorbent for Highly Efficient Removal of Methylene Blue from Water Pollution. *Sci. Total Environ.* **2018**, *628*−*629*, 959−968.
(21) Rahmanivahid, B.; Naderi, F.; Nayebzadeh, H. Removing Methyl Orange Molecules from Aqueous Medium by Magnetic Nanoparticles: Evaluating Adsorption Factors, Isotherms, Kinetics and Thermodynamics. *J. Water Environ. Nanotechnol.* **2020**, *5*, 1−16.
(22) Lei, C.; Pi, M.; Xu, D.; Jiang, C.; Cheng, B. Fabrication of Hierarchical Porous ZnO-Al2O3 Microspheres with Enhanced Adsorption Performance. *Appl. Surf. Sci.* **2017**, *426*, 360−368.
(23) Li, C.; Xiong, Z.; Zhang, J.; Wu, C. The Strengthening Role of the Amino Group in Metal-Organic Framework MIL-53 (Al) for Methylene Blue and Malachite Green Dye Adsorption. *J. Chem. Eng. Data* **2015**, *60*, 3414−3422.
(24) Zhao, J.; Xu, L.; Su, Y.; Yu, H.; Liu, H.; Qian, S.; Zheng, W.; Zhao, Y. Zr-MOFs Loaded on Polyurethane Foam by Polydopamine for Enhanced Dye Adsorption. *J. Environ. Sci.* **2021**, *101*, 177−188.
(25) Cojocaru, C.; Samoila, P.; Pascariu, P. Chitosan-Based Magnetic Adsorbent for Removal of Water-Soluble Anionic Dye: Artificial Neural Network Modeling and Molecular Docking Insights. *Int. J. Biol. Macromol.* **2019**, *123*, 587−599.
(26) Ayad, M.; Zaghlol, S. Nanostructured Crosslinked Polyaniline with High Surface Area: Synthesis, Characterization and Adsorption for Organic Dye. *Chem. Eng. J.* **2012**, *204*−*206*, 79−86.
(27) Chafai, H.; Laabd, M.; Elbariji, S.; Bazzaoui, M.; Albourine, A. Study of Congo Red Adsorption on the Polyaniline and Polypyrrole. *J. Dispersion Sci. Technol.* **2016**, *38*, 832−836.
(28) Agarwal, S.; Sadegh, H.; Monajjemi, M.; Hamdy, A. S.; Ali, G. A. M.; Memar, A. O. H.; Shahryari-Ghoshekandi, R.; Tyagi, I.; Gupta, V. K. Efficient Removal of Toxic Bromothymol Blue and Methylene Blue from Wastewater by Polyvinyl Alcohol. *J. Mol. Liq.* **2016**, *218*, 191−197.
(29) Dutta, S.; Gupta, B.; Srivastava, S. K.; Gupta, A. K. Recent Advances on the Removal of Dyes from Wastewater Using Various Adsorbents: A Critical Review. *Mater. Adv.* **2021**, *2*, 4497−4531.
(30) Sivadas, D. L.; Vijayan, S.; Rajeev, R.; Ninan, K. N.; Prabhakaran, K. Nitrogen-Enriched Microporous Carbon Derived from Sucrose and Urea with Superior CO2 Capture Performance. *Carbon* **2016**, *109*, 7−18.
(31) Hayeeye, F.; Sattar, M.; Chinpa, W.; Sirichote, O. Kinetics and Thermodynamics of Rhodamine B Adsorption by Gelatin/Activated Carbon Composite Beads. *Colloids Surf., A* **2017**, *513*, 259−266.
(32) Rashid, J.; Tehreem, F.; Rehman, A.; Kumar, R. Synthesis Using Natural Functionalization of Activated Carbon from Pumpkin Peels for Decolourization of Aqueous Methylene Blue. *Sci. Total Environ.* **2019**, *671*, 369−376.
(33) Tyagi, A.; Banerjee, S.; Singh, S.; Kar, K. K. Biowaste Derived Activated Carbon Electrocatalyst for Oxygen Reduction Reaction: Effect of Chemical Activation. *Int. J. Hydrogen Energy* **2020**, *45*, 16930−16943.
(34) Wang, Y.; Wang, F.; Wan, T.; Cheng, S.; Xu, G.; Cao, R.; Gao, M. Enhanced Adsorption of Pb(II) Ions from Aqueous Solution by Persimmon Tannin-Activated Carbon Composites. *J. Wuhan Univ. Technol., Mater. Sci. Ed.* **2013**, *28*, 650−657.
(35) Kim, H. S.; Kang, M. S.; Lee, S.; Lee, Y. W.; Yoo, W. C. N-Doping and Ultramicroporosity-Controlled Crab Shell Derived Carbons for Enhanced CO2 and CH4 Sorption. *Microporous Mesoporous Mater.* **2018**, *272*, 92−100.
(36) Liu, X.; He, C.; Yu, X.; Bai, Y.; Ye, L.; Wang, B.; Zhang, L. Net-like Porous Activated Carbon Materials from Shrimp Shell by

https://doi.org/10.1021/acsomega.3c00339
ACS Omega 2023, 8, 16158−16173

Solution-Processed Carbonization and H3PO4 Activation for Methylene Blue Adsorption. *Powder Technol.* **2018**, *326*, 181−189.
(37) Masoumi, S.; Dalai, A. K. Optimized Production and Characterization of Highly Porous Activated Carbon from Algal-Derived Hydrochar. *J. Cleaner Prod.* **2020**, *263*, No. 121427.
(38) Rehman, A.; Park, S. J. Environmental Remediation by Microporous Carbon: An Efficient Contender for CO2 and Methylene Blue Adsorption. *J. CO2 Util.* **2019**, *34*, 656−667.
(39) Xu, L.; Guo, L.; Hu, G.; Chen, J.; Hu, X.; Wang, S.; Dai, W.; Fan, M. Nitrogen-Doped Porous Carbon Spheres Derived from D-Glucose as Highly-Efficient CO2 Sorbents. *RSC Adv.* **2015**, *5*, 37964−37969.
(40) Sekhon, S. S.; Kaur, P.; Park, J. S. From Coconut Shell Biomass to Oxygen Reduction Reaction Catalyst: Tuning Porosity and Nitrogen Doping. *Renewable Sustainable Energy Rev.* **2021**, *147*, No. 111173.
(41) Kundu, S.; Chowdhury, I. H.; Naskar, M. K. Nitrogen-Doped Nanoporous Carbon Nanospheroids for Selective Dye Adsorption and Pb(II) Ion Removal from Waste Water. *ACS Omega* **2018**, *3*, 9888−9898.
(42) Zhou, Q.; Chen, W.; Jiang, X.; Liu, H.; Ma, S.; Wang, B. Preparation of a Novel Nitrogen-Containing Graphitic Mesoporous Carbon for the Removal of Acid Red 88. *Sci. Rep.* **2020**, *10*, No. 1353.
(43) Hou, Y.; Yan, S.; Huang, G.; Yang, Q.; Huang, S.; Cai, J. Fabrication of N-Doped Carbons from Waste Bamboo Shoot Shell with High Removal Efficiency of Organic Dyes from Water. *Bioresour. Technol.* **2020**, *303*, No. 122939.
(44) Wang, B.; Zhai, Y.; Wang, T.; Li, S.; Peng, C.; Wang, Z.; Li, C.; Xu, B. Fabrication of Bean Dreg-Derived Carbon with High Adsorption for Methylene Blue: Effect of Hydrothermal Pretreatment and Pyrolysis Process. *Bioresour. Technol.* **2019**, *274*, 525−532.
(45) Przepiórski, J.; Skrodzewicz, M.; Morawski, A. W. High Temperature Ammonia Treatment of Activated Carbon for Enhancement of CO2 Adsorption. *Appl. Surf. Sci.* **2004**, *225*, 235−242.
(46) Wu, B.; Meng, H.; Morales, D. M.; Zeng, F.; Zhu, J.; Wang, B.; Risch, M.; Xu, Z. J.; Petit, T. Nitrogen-Rich Carbonaceous Materials for Advanced Oxygen Electrocatalysis: Synthesis, Characterization, and Activity of Nitrogen Sites. *Adv. Funct. Mater.* **2022**, *32*, No. 2204137.
(47) Iqbal, S.; Rasheed, T.; Bilal, M.; Shah, K. H.; Bilal, M.; Sherazi, T. A. Biomass-Derived Nitrogen-Rich Porous Carbon Composite for Supercapacitor Application. *J. Mater. Sci.: Mater. Electron.* **2022**, *33*, 14793−14804.
(48) Nazir, G.; Rehman, A.; Hussain, S.; Afzal, A. M.; Dastgeer, G.; Rehman, M. A.; Akhter, Z.; Al-Muhimeed, T. I.; AlObaid, A. A. Heteroatoms-Doped Hierarchical Porous Carbons: Multifunctional Materials for Effective Methylene Blue Removal and Cryogenic Hydrogen Storage. *Colloids Surf., A* **2021**, *630*, No. 127554.
(49) Rothe, R.; Antonietti, M.; Fechler, N. The Bakery of High-End Sorption Carbons: Sugar−Urea Doughs as Processable Precursors for Functional Carbons. *J. Mater. Chem. A* **2017**, *5*, 16352−16358.
(50) Schaeperkoetter, J. C.; Connolly, M. J.; Buck, Z. N.; Taub, H.; Kaiser, H.; Wexler, C. Adsorption-Induced Expansion of Graphene Oxide Frameworks: Observation by in Situ Neutron Diffraction. *ACS Omega* **2019**, *4*, 18668−18676.
(51) Nie, F.; He, D.; Guan, J.; Bao, H.; Zhang, K.; Meng, T.; Zhang, Q. Influence of Temperature on the Product Distribution during the Fast Pyrolysis of Indonesian Oil Sands and the Relationships of the Products to the Oil Sand Organic Structure. *Energy Fuels* **2017**, *31*, 1318−1328.
(52) Fu, P.; Zhou, L.; Sun, L.; Huang, B.; Yuan, Y. Nitrogen-Doped Porous Activated Carbon Derived from Cocoon Silk as a Highly Efficient Metal-Free Electrocatalyst for the Oxygen Reduction Reaction. *RSC Adv.* **2017**, *7*, 13383−13389.
(53) Inglezakis, V. J. Solubility-Normalized Dubinin−Astakhov Adsorption Isotherm for Ion-Exchange Systems. *Microporous Mesoporous Mater.* **2007**, *103*, 72−81.
(54) Alberti, G.; Amendola, V.; Pesavento, M.; Biesuz, R. Beyond the Synthesis of Novel Solid Phases: Review on Modelling of Sorption Phenomena. *Coord. Chem. Rev.* **2012**, *256*, 28−45.
(55) Ma, Y. Comparison of Activated Carbons Prepared from Wheat Straw via ZnCl2 and KOH Activation. *Waste Biomass Valorization* **2017**, *8*, 549−559.
(56) Chen, Y.; Zhai, S. R.; Liu, N.; Song, Y.; An, Q. D.; Song, X. W. Dye Removal of Activated Carbons Prepared from NaOH-Pretreated Rice Husks by Low-Temperature Solution-Processed Carbonization and H3PO4 Activation. *Bioresour. Technol.* **2013**, *144*, 401−409.
(57) Girgis, B. S.; Yunis, S. S.; Soliman, A. M. Characteristics of Activated Carbon from Peanut Hulls in Relation to Conditions of Preparation. *Mater. Lett.* **2002**, *57*, 164−172.
(58) Rashid, R. A.; Jawad, A. H.; Ishak, M. A. M.; Kasim, N. N. KOH-Activated Carbon Developed from Biomass Waste: Adsorption Equilibrium, Kinetic and Thermodynamic Studies for Methylene Blue Uptake. *Desalin. Water Treat.* **2016**, *57*, 27226−27236.
(59) Hassan, A. F.; Elhadidy, H. Production of Activated Carbons from Waste Carpets and Its Application in Methylene Blue Adsorption: Kinetic and Thermodynamic Studies. *J. Environ. Chem. Eng.* **2017**, *5*, 955−963.
(60) Jawad, A. H.; Saud Abdulhameed, A.; Wilson, L. D.; Syed-Hassan, S. S. A.; Alothman, Z. A.; Rizwan Khan, M. High Surface Area and Mesoporous Activated Carbon from KOH-Activated Dragon Fruit Peels for Methylene Blue Dye Adsorption: Optimization and Mechanism Study. *Chin. J. Chem. Eng.* **2021**, *32*, 281−290.
(61) Tuli, F. J.; Hossain, A.; Kibria, A. K. M. F.; Tareq, A. R. M.; Mamun, S. M. M. A.; Ullah, A. K. M. A. Removal of Methylene Blue from Water by Low-Cost Activated Carbon Prepared from Tea Waste: A Study of Adsorption Isotherm and Kinetics. *Environ. Nanotechnol., Monit. Manage.* **2020**, *14*, No. 100354.
(62) Jawad, A. H.; Abdulhameed, A. S.; Bahrudin, N. N.; Hum, N. N. M. F.; Surip, S. N.; Syed-Hassan, S. S. A.; Yousif, E.; Sabar, S. Microporous Activated Carbon Developed from KOH Activated Biomass Waste: Surface Mechanistic Study of Methylene Blue Dye Adsorption. *Water Sci. Technol.* **2021**, *84*, 1858−1872.
(63) Jawad, A. H.; Saber, S. E. M.; Abdulhameed, A. S.; Reghioua, A.; Alothman, Z. A.; Wilson, L. D. Mesoporous Activated Carbon from Mangosteen (Garcinia Mangostana) Peels by H3PO4 Assisted Microwave: Optimization, Characterization, and Adsorption Mechanism for Methylene Blue Dye Removal. *Diamond Relat. Mater.* **2022**, *129*, No. 109389.
(64) Tran, T. H.; Le, H. H.; Pham, T. H.; Nguyen, D. T.; La, D. D.; Chang, S. W.; Lee, S. M.; Chung, W. J.; Nguyen, D. D. Comparative Study on Methylene Blue Adsorption Behavior of Coffee Husk-Derived Activated Carbon Materials Prepared Using Hydrothermal and Soaking Methods. *J. Environ. Chem. Eng.* **2021**, *9*, No. 105362.
(65) Jawad, A. H.; Sahu, U. K.; Mastuli, M. S.; Alothman, Z. A.; Wilson, L. D. Multivariable Optimization with Desirability Function for Carbon Porosity and Methylene Blue Adsorption by Watermelon Rind Activated Carbon Prepared by Microwave Assisted H3PO4. *Biomass Convers. Biorefin.* **2022**, 1−15.
(66) Jawad, A. H.; Abdulhameed, A. S. Statistical Modeling of Methylene Blue Dye Adsorption by High Surface Area Mesoporous Activated Carbon from Bamboo Chip Using KOH-Assisted Thermal Activation. *Energy Ecol. Environ.* **2020**, *5*, 456−469.
(67) Jawad, A. H.; Mohd Firdaus Hum, N. N.; Abdulhameed, A. S.; Mohd Ishak, M. A. Mesoporous Activated Carbon from Grass Waste via H3PO4-Activation for Methylene Blue Dye Removal: Modelling, Optimisation, and Mechanism Study. *Int. J. Environ. Anal. Chem.* **2020**, *102*, 6061−6077.
(68) Medhat, A.; El-Maghrabi, H. H.; Abdelghany, A.; Abdel Menem, N. M.; Raynaud, P.; Moustafa, Y. M.; Elsayed, M. A.; Nada, A. A. Efficiently Activated Carbons from Corn Cob for Methylene Blue Adsorption. *Appl. Surf. Sci. Adv.* **2021**, *3*, No. 100037.
(69) Mbarki, F.; Selmi, T.; Kesraoui, A.; Seffen, M. Low-Cost Activated Carbon Preparation from Corn Stigmata Fibers Chemically Activated Using H3PO4, ZnCl2 and KOH: Study of Methylene Blue

https://doi.org/10.1021/acsomega.3c00339
ACS Omega 2023, 8, 16158−16173

Adsorption, Stochastic Isotherm and Fractal Kinetic. *Ind. Crops Prod.* **2022**, *178*, No. 114546.

https://doi.org/10.1021/acsomega.3c00339
ACS Omega 2023, 8, 16158−16173